UCSF

UC San Francisco Electronic Theses and Dissertations

Title

Simultaneous Visualization of Arteries, Veins, and Cerebral Microbleeds from 7T MRA-SWI Images for Assessing the Effects of Radiation Therapy on the Brain

Permalink

https://escholarship.org/uc/item/9gn6c0h0

Author

Avadiappan, Sivakami

Publication Date

2017

Peer reviewed|Thesis/dissertation

Simultaneous Visualization of Arteries, Veins, and Cerebral
Microbleeds from 7T MRA-SWI Images for Assessing the Effects of
Radiation Therapy on the Brain

by

Sivakami Avadiappan

THESIS

Submitted in partial satisfaction of the requirements for the degree of

MASTER OF SCIENCE

in

Biomedical Imaging

in the

GRADUATE DIVISION

of the

UNIVERSITY OF CALIFORNIA, SAN FRANCISCO

Acknowledgments

I am very grateful to my supervisor Dr. Janine Lupo whose expertise, guidance and support made it possible for me to work on a topic that was of great interest to me. I am largely indebted to Dr. Melanie Morrison for helping me get familiarized with the lab and patiently answering my questions. I would like to thank Angela Jakary for helping in data acquisition and compiling essential clinical data. Special thanks to Dr. Sam Payabvash for providing valuable insight in analyzing brain images. I would like to thank Dr. Christopher Hess, Dr. David Saloner, and Dr. Duan Xu for taking time out of their hectic schedules to be a part of my thesis committee and provide feedback. Thank you to all members in Lupo lab for their advice and input during the study. Additional thanks to the MSBI program administrators and faculty for providing me this wonderful education. Finally, thank you to my classmates for making this program an enjoyable experience.

Dedication

I would like to dedicate this to my family for providing moral and financial support.

Simultaneous Visualization of Arteries, Veins, and Cerebral Microbleeds from 7T MRA-SWI Images for Assessing the Effects of Radiation Therapy on the Brain

Sivakami Avadiappan

Abstract

The use of radiation therapy for treatment of brain tumor is controversial due to its long-term effects on neurocognitive function, especially in pediatric patients. Developing objective criteria for evaluating the severity of radiation-related injury is critical for children, due to their longer survival times and impact on early cognitive development. Cerebral microbleeds (CMB) which are deposits of hemosiderin that initially accumulate around vessels and can appear as early as 6 months post radiation therapy and continue to increase in number over time, however their vascular etiology is unknown. The aim of this project is to develop a method for simultaneous visualization of arteries, veins, and CMBs in order to automatically calculate vascular metrics from the fusion of MRA and SWI images obtained from a multi echo sequence at 7 Tesla. A strategy to assess the distribution of CMB's relative to surrounding arteries and veins would help establish a connection between CMB formation and underlying vascular pathology. The tools developed in this study will be evaluated in pediatric patients with CMBs who have been treated with uniform supratentorial cranial radiation therapy for childhood brain tumors in order to ultimately determine whether metrics describing vascular structure could serve as quantitative markers for radiation injury, help in identifying regions of the brain that are most susceptible to radiation, and predict the formation of new CMBs and subsequent cognitive impairment.

Table of Contents

List of Figures

List of Tables

CHAPTER 1

INTRODUCTION

1.1 Background

Central nervous system tumors account for almost 20 percent of all childhood cancers [1]. They are the second most common form of childhood cancer after leukemia. An estimated 4,830 new cases of childhood CNS tumors are expected to be diagnosed in 2017 in the US alone [2]. The treatment options for pediatric brain tumor include surgery, chemotherapy and radiation therapy. Surgery is usually the first step, following which children may need radiation therapy or chemotherapy. External beam radiation therapy is applied to the area around the surgical cavity to kill the tumor cells that remain after surgery. In certain aggressive cancers with a propensity for disseminated recurrence, such as medulloblastoma -- the most common type of childhood brain tumor -- the standard of care includes whole brain radiation therapy to be either 24 or 36Gy in addition to the site where the primary tumor is located. Radiation therapy may also be used to treat tumors in cases where surgery is not considered safe. However, radiation therapy has known long term side effects in pediatric patients that include attention deficits, reduced performance of working memory, and deficits in executive function and verbal memory [3-6].

At the microscopic level, the histologic response to radiation initially varies depending on the timing of analysis relative to exposure. Early alterations after radiation include vascular changes as well as white matter pathology ranging from demyelination to coagulative necrosis, cortical atrophy and endothelial proliferation [7]. Late toxicities of radiation include cognitive deficits, neuroendocrine changes, cavernous malformations, atherosclerosis, small vessel

occlusive disease and cerebral microbleeds (CMBs). The incidence of neurovascular events in this population is 100-fold higher than in the general pediatric population [8].

CMBs are MRI defined lesions corresponding to small deposits of blood products (mainly hemosiderin) from previous episodes of bleeding in the brain, related to small vessel damage [9]. CMBs appear as small hypointense spherical lesions on SWI as shown in Figure 1. CMBs initially accumulate around vessels and can appear as early as 8 months post radiation therapy and continue to increase in number over time, however their vascular etiology is unknown [10]. CMBs have been proposed as a potential biomarker for neurocognitive impairment following radiation therapy. In a study by Roddy et al [10], it was found that CMB's have a cumulative incidence of 48% at 5 years. Also, children who had whole brain irradiation developed 4 times more CMB's than those treated with focal irradiation. The prevalence of CMBs in different brain locations does indicate the brain areas most likely to be affected and should match the observed pattern of cognitive deficits. CMB's in the frontal lobe affect the Groton Maze Learning (GML) test, while CMB's in temporal lobe affects verbal memory. Presently studies are also being conducted to see how CMBs evolve over time.
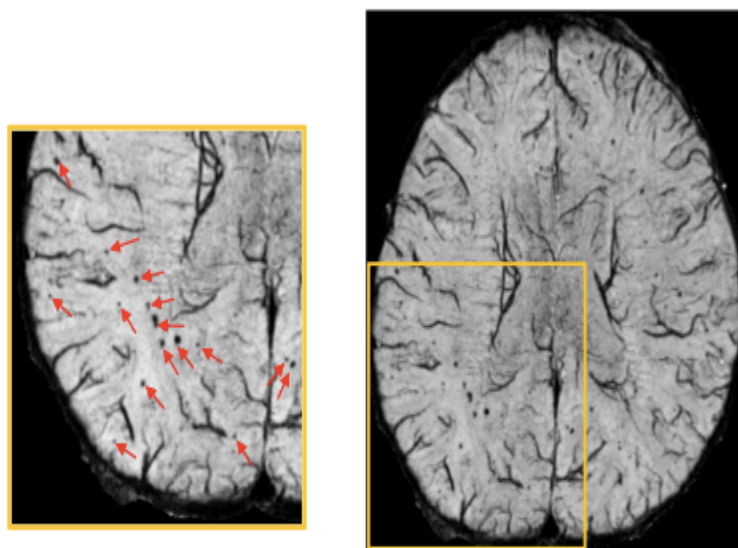

Figure 1: CMBs appear as small hypo-intense spherical lesions on SWI

1.2 Motivation

The extent of neurocognitive decline varies from patient to patient, depending on factors such as tumor location and presence of hydrocephalus [11-14]. Despite longer survival rates, many patients will not maximize their cognitive potential or lead an independent life as a result of childhood radiation therapy. Developing objective criteria for evaluating the severity of radiation related injury is critical for children, due to their long survival times and evolving cognitive development. The population at risk for these complications continues to increase because brain tumors are the most common solid tumors of childhood and the length of survival is increasing (5 year survival of 73.8%) [15]. With the improved long-term survival, understanding the late effects of the treatment is very important.

Since CMBs are considered to be areas containing hemosiderin deposits from previous bleeding close to damaged arterioles [9], investigating the characteristics of vasculature near the location of CMBs as well as the overall changes in vasculature as a result of radiation induced injury is of great interest. Brain artery diameters could serve as a risk factor for vascular events [16]. Small peripheral artery luminal diameter has been used as a surrogate marker of arteriopathy [17]. In clinical practice, diameters are often visually estimated from MR angiograms but determination of true diameters is very subjective. Diameter estimations by direct visualization depend on the contrast and resolution of the image. Thus an objective criterion is necessary for accurate diameter estimation to exclude subjectivity. In this work, we adopted a similar approach to that in the study by Dury et al [18] that used the Euclidean Distance Transform (EDT) to obtain a vessel thickness map for patients with Huntington's disease and compared it to healthy volunteers. It is hypothesized that radiation-induced damage to the microvasculature will result in a pruning of small vessels and a shift in vessel radii distribution towards smaller vessel diameters.

1.3 TOF- MRA (Time of Flight Magnetic Resonance Angiography)

MRA is a technique to visualize flow within arteries without administering contrast. It is based on the phenomenon of flow-related enhancement of spins entering an imaging slice. These spins have more signal than the surrounding stationary spins because they enter the slice with full magnetization. Flow compensated gradient-echo sequences are optimized to enhance the vascular signal over that of the background tissues in two ways- (a) Saturating the stationary tissue signal with short TR, as the longitudinal magnetization of these tissues does not have time to fully recover and their signal weakens (b) Utilizing the inflow effect -The signal from the blood flow has not been saturated and is thus stronger than that of the saturated background tissues. From the reconstructed image volume, a Maximum Intensity Projection (MIP) for the entire volume is typically generated for clinical evaluation, which gives a 2D angiographic appearance as shown in Figure 2.
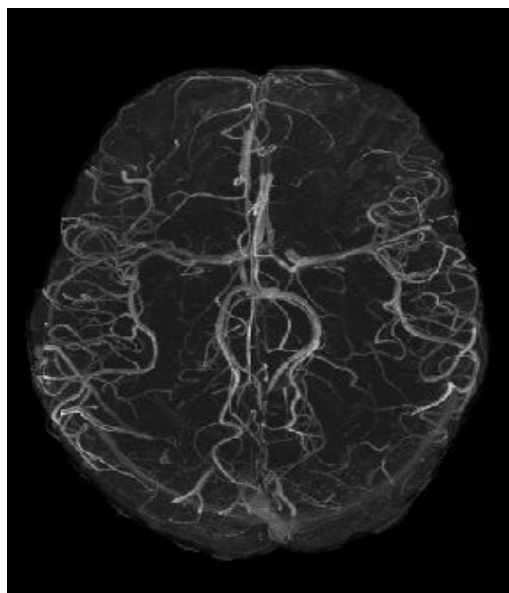

Figure 2: 2D Maximum Intensity Projection of MRA

1.4 SWI (Susceptibility Weighted Imaging)

SWI is a powerful tool to visualize veins and CMBs. Susceptibility-weighted images are created by weighting the hypointense voxels of the magnitude image of a T2*-weighted sequence by a weighted phase mask in order to increase contrast. 7T imaging provides heightened sensitivity to detect CMBs, which appear as hypointense spherical lesions on SWI. Compounds that have paramagnetic, diamagnetic, and ferromagnetic properties all interact with the local magnetic field distorting it, thus, altering the phase of local tissue and results in loss of signal. The most common use of SWI is for the identification of blood products and calcium, both of which may not be obvious on other MRI sequences. However, distinguishing between calcification and blood products is not possible on the post-processed SWI images as both exhibit signal dropout and blooming. The filtered phase images, however, are able to distinguish the two, as diamagnetic and paramagnetic compounds will result in opposing phase shifts. From the SWI image volume, minimum Intensity Projections (mIP) are typically obtained through 8-10mm thick slices. A single 8mm projected SWI slice from a patient with radiation-induced CMBs is shown in Figure 3.
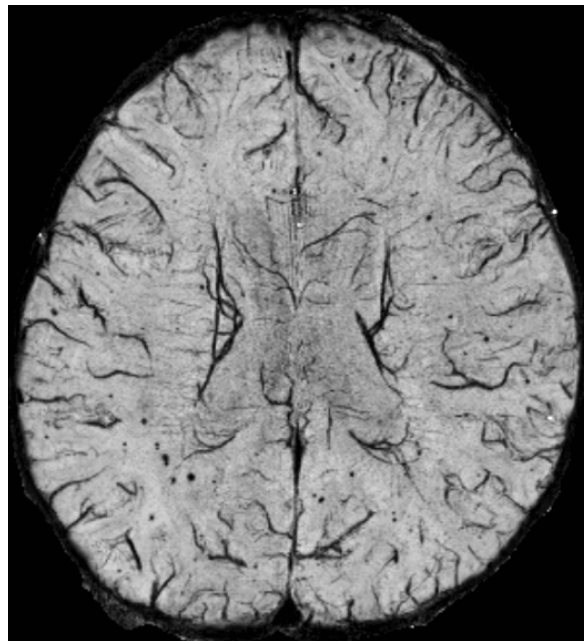

Figure 3: Single slice from 8mm SWI mIP projection

1.5 Multi-echo TOF-SWI sequence

A four-echo, gradient echo sequence [19] has been previously developed to simultaneously image arteries, veins and CMBs, obviating the need for image co-registration and reducing the scanning time. As shown in Figure 4, the first echo is used to create TOF-MRA images and the remaining three echoes are combined to create a composite SWI image. This multi-echo sequence eliminates the need for co-registration, which causes blurring of the sub-millimeter CMBs and microvasculature, facilitating more accurate quantification of smaller vascular structures.
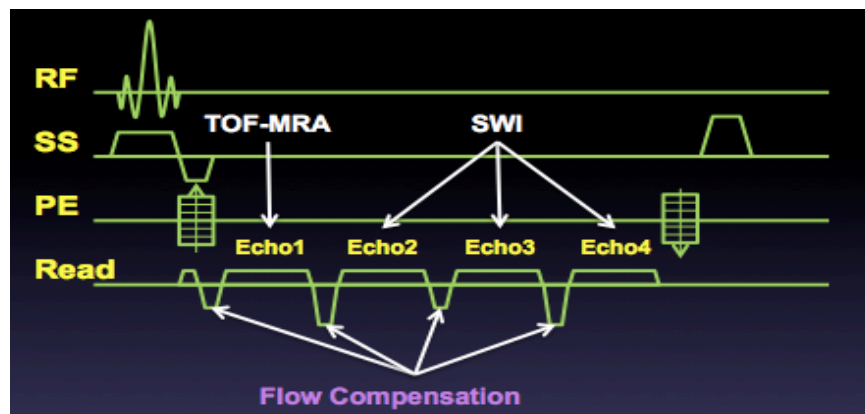
Figure 4: Novel multi-echo TOF-MRA/SWI sequence

1.6 Objective

The goal of this thesis is to develop robust, semi-automatic processing pipelines for 1) the accurate segmentation of arteries from MRA images, 2) the simultaneous visualization of arteries, veins and CMBs, and 3) the quantification of vessel thickness. Once developed and implemented, the goal is for larger-scale application of these tools to understand the relationship between CMB formation and vessel thinning, and to assess the global and focal effects of radiation therapy on microvasculature.

CHAPTER 2

MATERIALS AND METHODS

2.1 Study Population

Preliminary analysis was performed on data from a subset of five pediatric patients with medulloblastomas and two healthy volunteers. These patients are part of the Rad-Art (Radiation induced Arteriopathy) study, which is a cohort study of childhood cancer survivors following radiation therapy. The advanced 7T imaging component of this study is ongoing and has thus far accumulated imaging data from 20 pediatric patients (Age: 10-24 years) who have been treated with whole-brain CRT 0.75-15 years prior. A control group was also included, consisting of 3 pediatric patients who did not receive radiation therapy.

2.2 Data Acquisition

All patients and volunteers were imaged using a 7T MRI scanner (GE Healthcare, Wisconsin) with a 32-channel phased-array coil (NOVA Medical, Massachusetts). The multi-echo MRA-SWI sequence described previously was used to acquire images. These images had a voxel size of 0.46 x 0.46 x 1 mm with an in plane 512 x 384 matrix, a FOV of 24 cm and slice thickness of 1mm. A TR of 40 ms and 4 TEs of 2.7, 10.5, 13.2 and 20.9 ms were utilized. Flow compensation was performed only in the readout direction, and echoes were partially acquired with 65% partial Fourier sampling. A flip angle of 25 degrees was used and a multiple overlapping thin-slab acquisition was employed. Three 36 mm slabs partitioned into 1-mm thick slices with 12 slices of overlap were used. The acquisition was accelerated in the phase encoding direction with an acceleration factor of 3, resulting in an acquisition time of 10.6 min. Additionally, T1-weighted IR-SPGR MRI images were obtained for anatomical reference.

2.3 Post Processing

Raw k-space data from the 32 coils was transferred off-line to a Linux workstation (Sun Microsystems, Mountain View, CA), where post-processing was done using in-house programs written with MATLAB software. The processing pipeline for the reconstruction of the multi-echo data after parallel imaging is illustrated in Figure 5. Partially acquired k-space samples were reconstructed to full size using Projection onto convex sets (POCS). Zero padding in the phase-encoding direction was done to create a 512 x 512 matrix. Magnitude images from each coil were combined using the root sum of squares [20] and skull stripping was done using FMRIB Software Library (FSL) Brain Extraction Tool (BET) [21]. The magnitude images for the first echo was used for MRA and the final three echoes were used for SWI processing as described below.
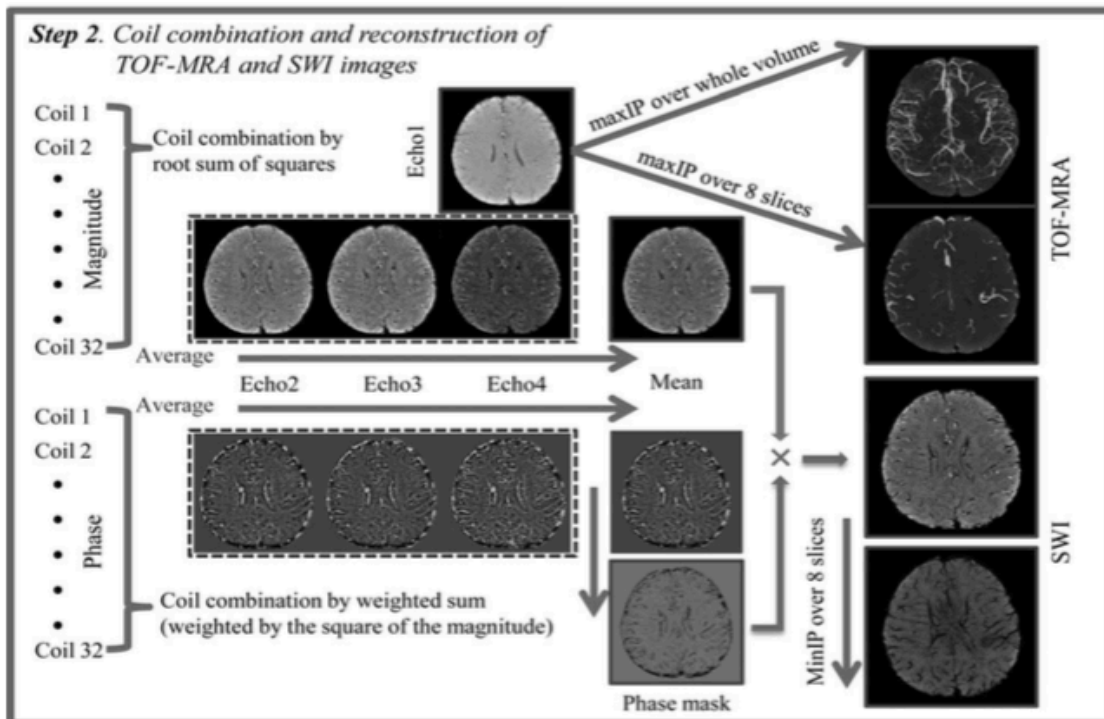

Figure 5: Processing pipeline for the reconstruction of the multi-echo data

In order to generate the SWI images, high pass filtering was first done on the phase images for each coil. This is because phase is also sensitive to unwanted magnetic field inhomogeneity, eddy current effects and air-tissue interface effects. The size of the Hanning filter was set as 72, 88 and 104 for the echoes 2, 3 and 4 respectively. The high pass filtered phase image from each coil was combined by weighting by the square of the corresponding magnitude intensity. Averaging phase images from echoes 2-4 produces a mean phase image. A negative phase mask is then created by linearly scaling negative phase values between zero and one and setting positive phase values to one. This phase mask is multiplied 4 times with the mean magnitude image from echoes 2-4 to create the final composite SWI image. The skull and background were removed from reconstructed images by applying a brain mask created from the combined magnitude image with FSL's brain extraction tool software (Smith, 2002).

2.4 Vessel Enhancement Method for Segmentation of Arteries

A common problem with the maximum intensity projection is that small vessels with low contrast are hardly visible. A vessel enhancement method can remove small vessel delineation. In this study, a multi scale approach to vessel enhancement via eigenvalue analysis of the Hessian matrix as proposed by Frangi et al was used [22]. It is also called as the Frangi filter. A common approach to analyze the local behavior of an image L, is to consider its Taylor expansion in the neighborhood of the point x_o,

$$L(x_o + \delta x_{o,} s) \approx L(x_o, s) + \delta x_o^T \nabla_{o,s} + \delta x_o^T H_o \, \delta x_o \quad (1)$$

The above expansion approximates the image structure up to second order.

The partial derivatives are calculated as voxel intensity differences in the neighborhood of the voxel. In this framework, differentiation is defined as convolution with Derivative of Gaussian (DOG).

$$\frac{\partial}{\partial x} L(x, s) = s^r \, \mathrm{L}(\mathbf{x}) * \frac{\partial}{\partial x} G(x, s) \quad (2)$$

Where ^{r} is the Lindeberg parameter and the D-dimensional Gaussian function is defined as:

$$G(x,s) = \frac{1}{\sqrt{(2\pi s^2)^D}} e^{-\frac{\|x\|^2}{2s^2}} \qquad (3)$$

Where s is the standard deviation (scale) of the Gaussian kernel.

From equation 1, the second order directional derivative is

$$\delta x_o{}^T H_{o,\,s}\ \delta x_o = \left(\frac{\partial}{\partial \delta xo}\right)\left(\frac{\partial}{\partial \delta xo}\right) L(x_o,\,s) \qquad (4)$$

For each voxel of the input image, a Hessian matrix is obtained from second order partial derivatives of the image.

$$H_{o,\,s}\ U_{s,\,k} = \lambda_{s,k}\ U_{s,k} \qquad (5)$$

$$U^T{}_{s,k}\ H_{o,s}\ U_{s,k} = \lambda_{s,k} \qquad (6)$$

Analysis of eigenvalues of Hessian matrix

For the obtained Hessian matrix, its eigenvalues and eigenvectors are calculated. Eigen vector decomposition gives the orthonormal coordinate system that aligns with the second order structure of the image. It has been shown that [23] the eigenvector corresponding to the eigenvalue of the smallest magnitude determines the direction along the vessel i.e. direction of smallest intensity variations. A spherical neighborhood centered at xo is mapped onto an ellipsoid whose axes are the eigenvector directions and the respective eigenvalues are the axes semi-lengths. Eigen values are sorted so that λ1 < λ2< λ3. Table 1 summarizes the relations between and orientation of a structure in the image.

Table 1. Eigenvalues and corresponding structure orientation. Eigenvalues of Hessian matrix and image structure orientation (L=low, H +=high positive, H-= high negative)

2D		3D			
λ1	λ2	λ1	λ2	λ3	**Structure Orientation**
L	L	L	L	L	Noise (No preferred) structure
		L	L	H-	Bright plate like structure
		L	L	H+	Dark plate like structure
L	H-	L	H-	H-	Bright tubular structure
L	H+	L	H+	H+	Dark tubular structure
H-	H-	H-	H-	H-	Bright blob-like structure
H+	H+	H+	H+	H+	Dark blob-like structure

In MRA, vessels appear as bright tubular structures in a darker background. This prior information can be used as a consistency check to eliminate structures present in the dataset with a polarity different than the one sought. Hence, we need to look for structures whose λ_2 and λ_3 are both simultaneously negative. Thus, for an ideal tubular structure in MRA, $|\lambda_1| \approx 0$, $|\lambda_1| \ll |\lambda_2|$ and $\lambda_2 \approx \lambda_3$. Similarly, the same method when applied to the veins on an SWI image would have eigenvalues of the opposite polarity.

Several formulas were proposed to find the vessel score for a voxel [24-25]. Two geometric ratios are calculated from the second order ellipsoid [22]. The first ratio accounts for the deviation from blob-like structures, but does not distinguish between line and plate-like patterns. This ratio attains its maximum for a blob-like structure and is zero whenever $\lambda_1 \approx 0$, or λ_1 and λ_2 tend to vanish.

$$R_B = \frac{\text{Volume}/(\frac{4\pi}{3})}{\left(\text{Largest Cross Section} \frac{\text{Area}}{\pi}\right)^{\wedge}(\frac{3}{2})} = \frac{|\lambda_1|}{\sqrt{|\lambda_1 \lambda_3|}} \qquad (7)$$

The second ratio is defined as the largest cross-sectional area of the ellipsoid. This ratio accounts for the aspect ratio of the two largest second order derivatives. It can distinguish plate-like and line structures.

$$R_A = \frac{(\text{Largest Cross Section Area}/\pi)}{(\text{Largest Axis Semi}-\text{length})^{\wedge}2} = \frac{|\lambda_2|}{|\lambda_3|} \qquad (8)$$

The third term is computed as the magnitude of derivatives using the norm of the Hessian. Using the Frobenius matrix norm,

$$S = ||H||_F = \sqrt{\sum_{j \leq D} \lambda_j{}^2} \qquad (9)$$

This measure will be low in the background where no structure is present and the eigenvalues are small for the lack of contrast. The above-mentioned components are combined to define a vessel score that helps to distinguish vessels from non-vessels.

$$\mathcal{V}_o(s) = \begin{cases} 0 & \text{if } \lambda_2 > 0 \text{ or } \lambda_3 > 0, \\ (1 - \exp\left(-\frac{\mathcal{R}_A{}^2}{2\alpha^2}\right)) \exp\left(-\frac{\mathcal{R}_B{}^2}{2\beta^2}\right)(1 - \exp\left(-\frac{\mathcal{S}^2}{2c^2}\right)) \end{cases}$$

(10)

Where the parameter α controls edge thickness and β controls noise tolerance. Higher β is more tolerant to noise. The above steps are repeated for four sigma scales (1-4). Finally, scale optimization was done by integrating the vessel score at different scales.

$$V_o(Y) = \max_{s_{min} \leq s \leq s_{max}} V_o(s, Y) \tag{11}$$

The algorithm pipeline for the Hessian filter is shown in Figure 6.
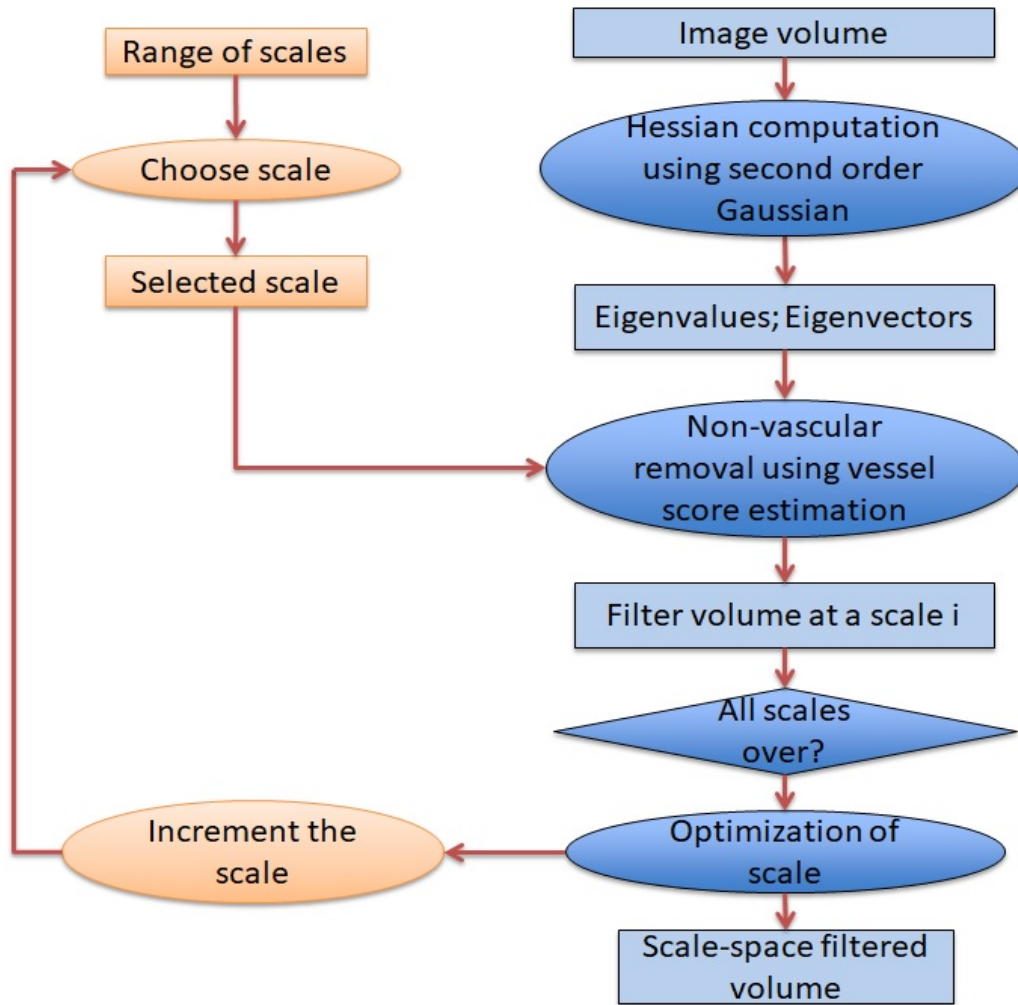

Figure 6: Pipeline for vessel enhancement based on Hessian method

2.4 Color overlays of vessels for visualization

Enhanced visualization of the arteries, CMBs, and veins on one image is necessary for the characterization of the mechanism of radiation induced vascular injury. Following artery enhancement, the Hessian filter was applied to the SWI images in order to enhance veins. CMB detection was done using an algorithm based on the fast radial symmetry transform, developed previously in our lab [26]. A MATLAB tool was created to generate color overlays of segmented arteries, veins, and CMBs on 8-mm thick SWI projections. The user can determine the color scheme so that proximity of CMBs to the nearest vessel and its corresponding thickness can be visualized.

2.5 Quantification of Vessel Thickness

In the Hessian based vessel enhancement method, it is observed that the thicker vessels tend to be narrower in the vessel enhancement image compared to the original image. This is because the vessel score is not very high at the boundaries. Thin vessels also appear to be a little broader than expected at the high scales. As a result, although the output of the vessel enhanced image helps with visualization, an alternate approach is necessary for the accurate quantification of vessel thickness. To solve this problem, we first apply an adaptive thresholding algorithm proposed by Bradley [27] to create a thresholded binary mask of vessels that can then be used as an input to our thickness quantification pipeline.

2.5.1 Euclidean Distance Transform (EDT)

The first step of our vessel thickness quantification pipeline applies a Euclidean distance transform to our thresholded binary images. The result of the transform is a gray level image that looks similar to the input image, except that the gray level intensities of points inside foreground regions are changed to show the distance to the closest boundary from each point. Euclidean distance is the distance metric used here to determine the distance between pixels. It has maximum value at the center of the vessel and minimum value at the boundaries as shown

in Figure 7. The centerline intensity of the EDT image gives the thickness of the vessel. A skeleton image is also obtained from the thresholded binary image. Multiplication of the skeleton with the EDT image gives the vessel radii map. The processing pipeline for obtaining the vessel thickness map is shown in Figure 8.

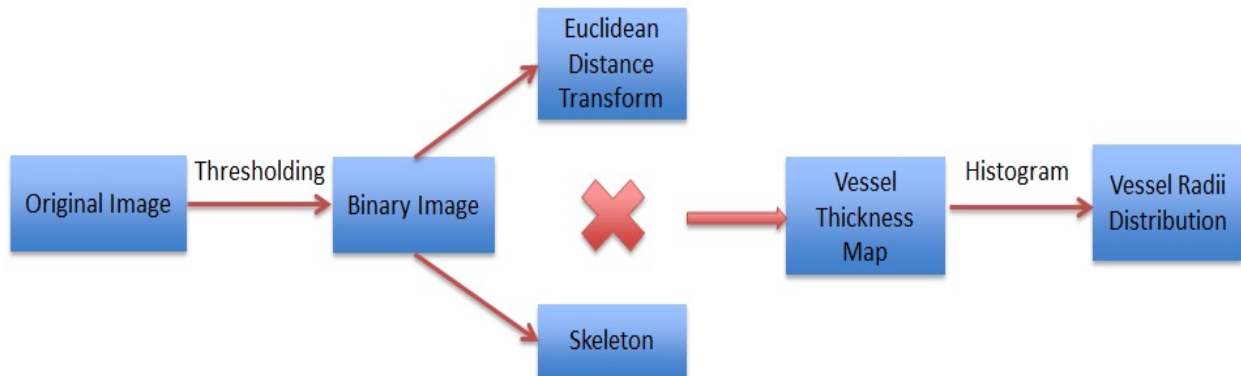**Figure 7. Vessel appears as a gradient with maximum value at the center and minimum at the boundaries after EDT**

Figure 8: The processing pipeline for obtaining the vessel thickness map

2.5.2 Repeatability of Vessel Thickness Map

One of the potential applications of vessel thickness map is to look for variations between serial scans in longitudinal studies. In that case, the thickness map could change between successive scans because of various subject-related parameters such as head orientation as well as imaging parameters such as slab placement. Hence in order to establish the amount of variability associated with this method, a volunteer was scanned twice within a interval of 3 weeks and the vessel radii distribution from the two scans were compared.

2.5.3 Vessel Radii Distribution Comparison Among Patients

Previous studies have shown that vessel radii depend on age and gender. Aging is associated with an increase in average radius and males consistently displayed higher average vessel radii compared to females across all age groups [28]. Hence, our preliminary demonstration of feasibility in patients compares histograms of vessel radii among subjects of similar age and gender who have varying numbers of CMBs.

CHAPTER 3

RESULTS

3.1 Hessian Filter Results

The Hessian filter results for the scales 1 to 4 is shown in Figure 9. It was found that combining the scales 2 and 3 gave the best results, as shown in Figure 10.
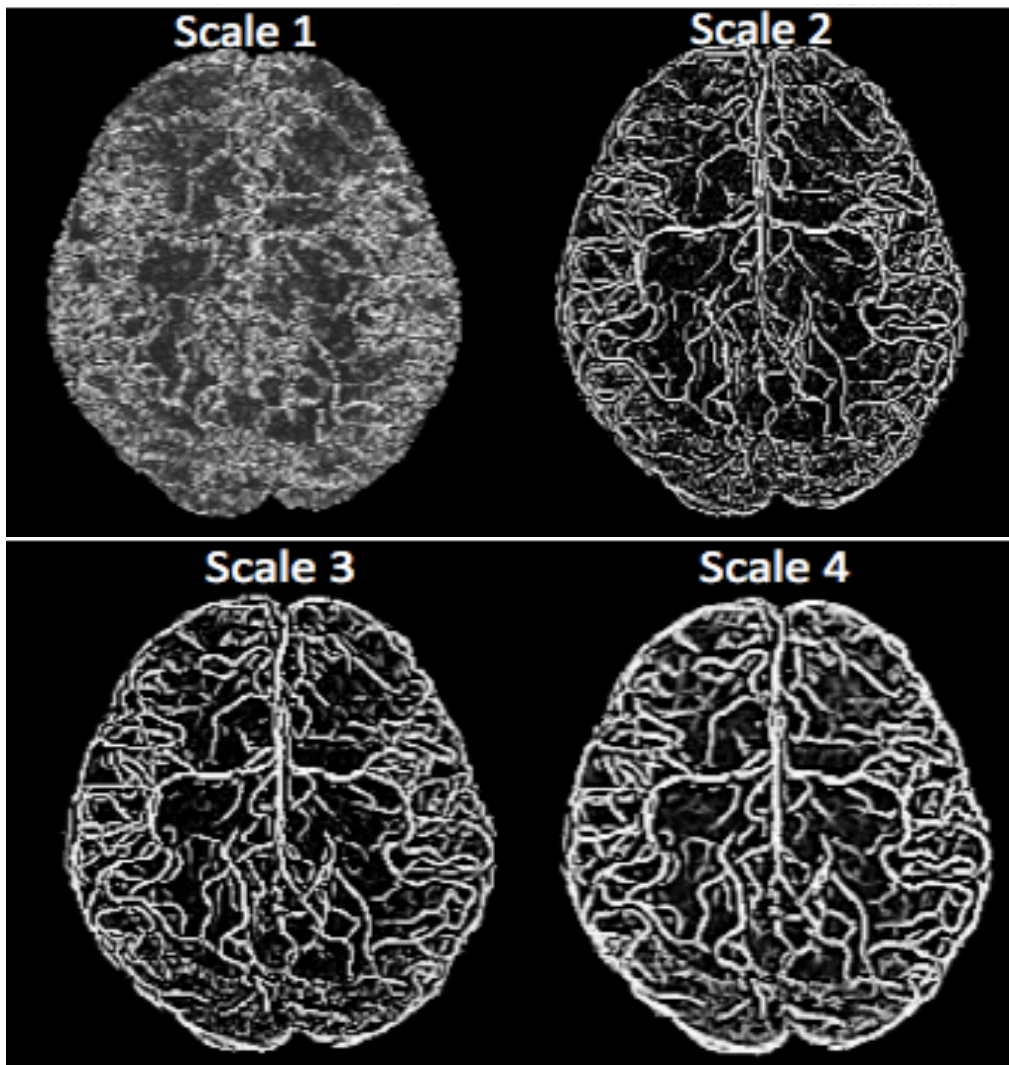

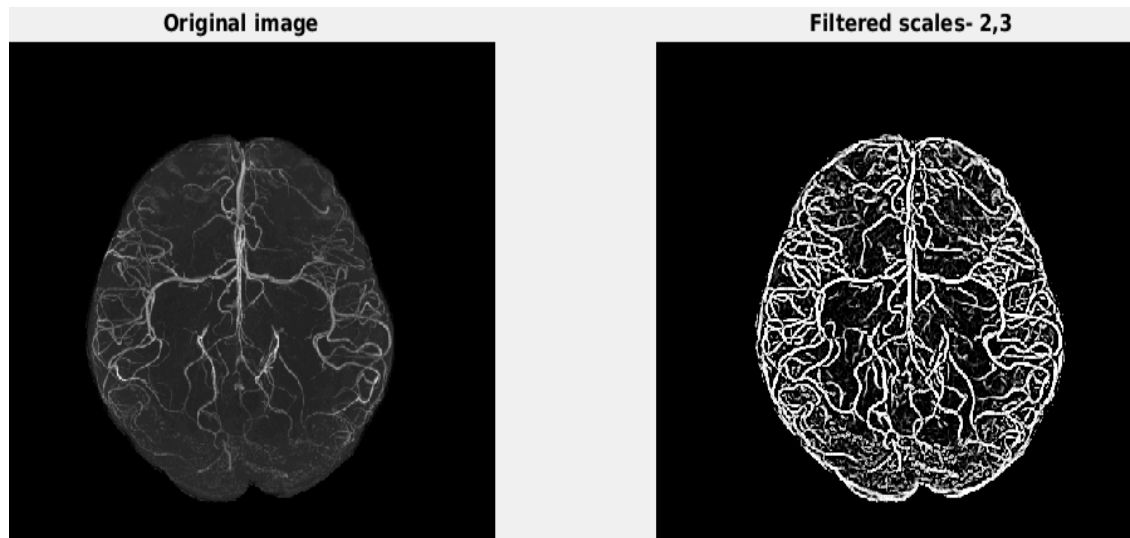**Figure 9: Results for different sigma values**

Figure 10: Original image and the Vessel enhanced image

The vessel enhancement technique applied to a single slice of 3D unprojected MRA data is shown in Figure 11(a) and the 8mm continuously projected MRA is shown in 11(b). The vessel enhancement technique applied to a single slice of 3D unprojected SWI is shown in Figure 11(c) and the 8mm continuously projected SWI is shown in 11 (d).
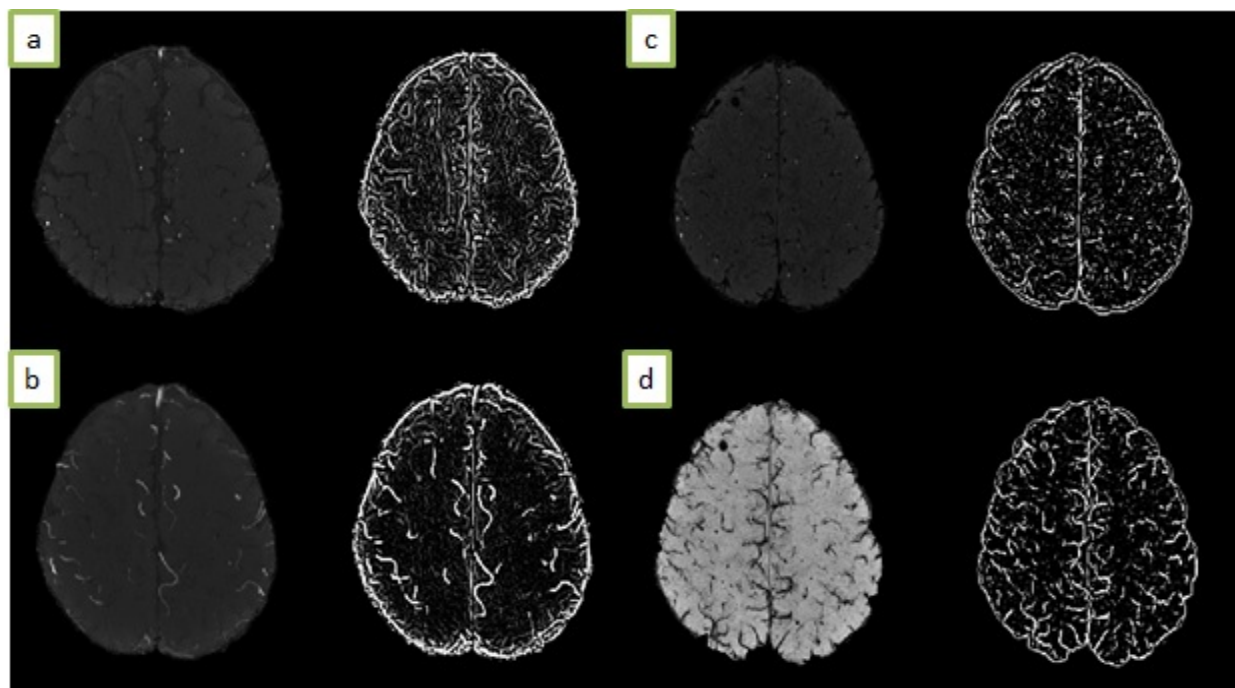

Figure 11: Hessian filter output for single slices

3.2 Color Overlay of Vessels

Figure 12(a) shows the color enhanced arteries overlaid on gray scale SWI. Figure 12(b) shows the CMBs marked in addition to the enhanced arteries. Figure 12(c) shows the veins extracted from the Hessian method (green color) overlaid on the arteries extracted from the Hessian method (red color) and CMBs (white color).
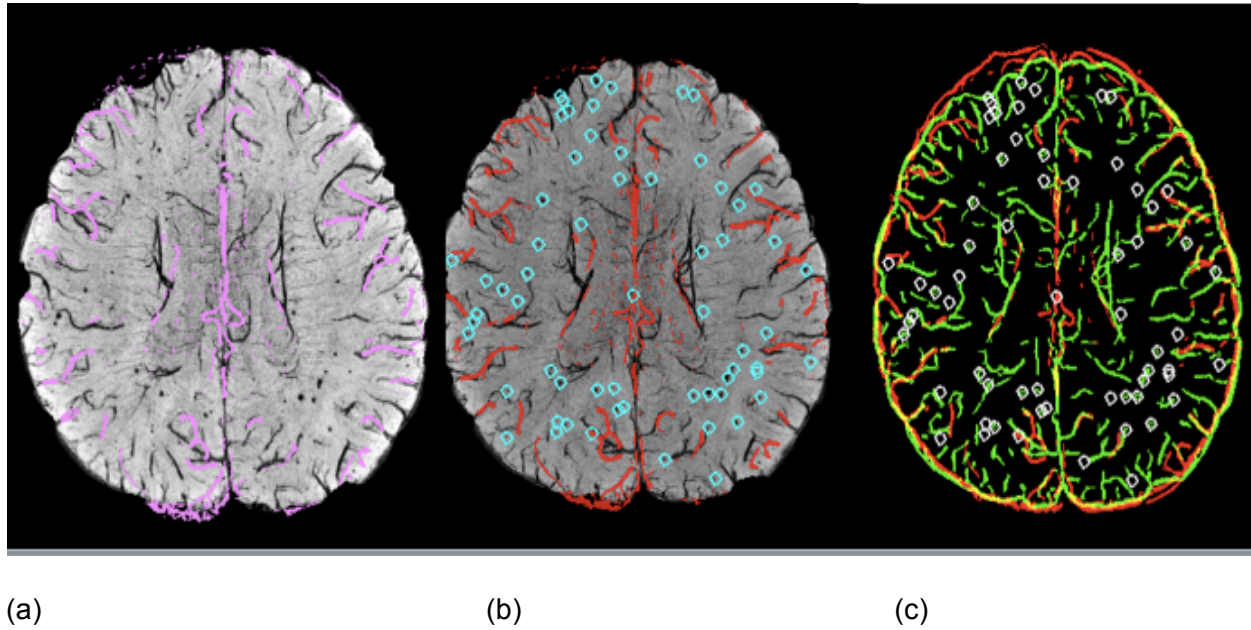

(a)   (b)   (c)

Figure 12: Overlay of enhanced arteries on SWI

3.3 Quantification of Vessel Thickness

The results of the different intermediate steps in obtaining the vessel thickness map is shown in Figure 13. Vessel radii distributions for the different sub regions of the brain can be obtained as shown in Figure 14 and 15. The x-axis of the histogram plot represents the radii of the vessel in terms of the number of pixels.
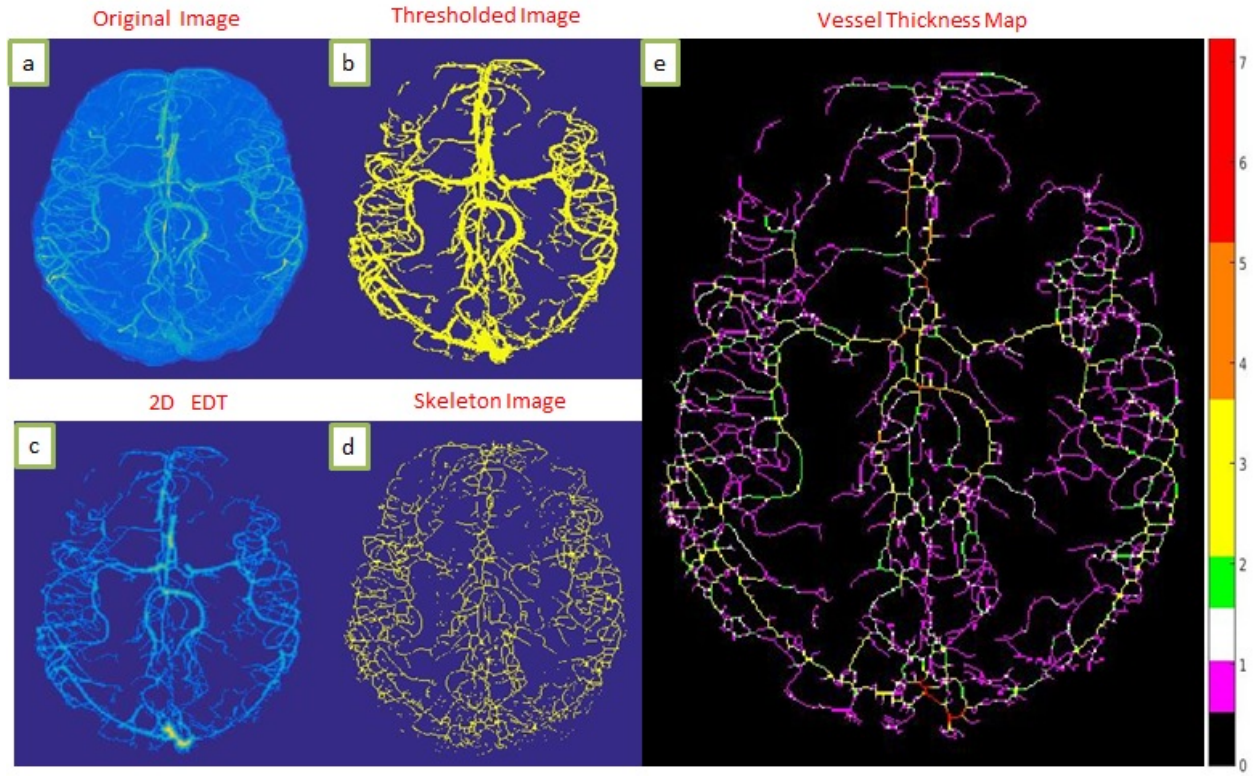
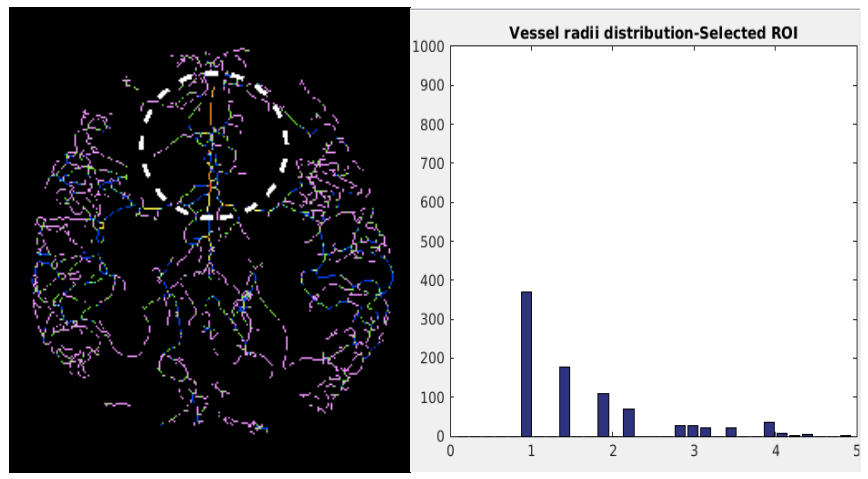**Figure 13: Intermediate steps in obtaining the vessel thickness map**

Figure 14: Vessel radii distribution for the different sub regions of the brain- ROI 1
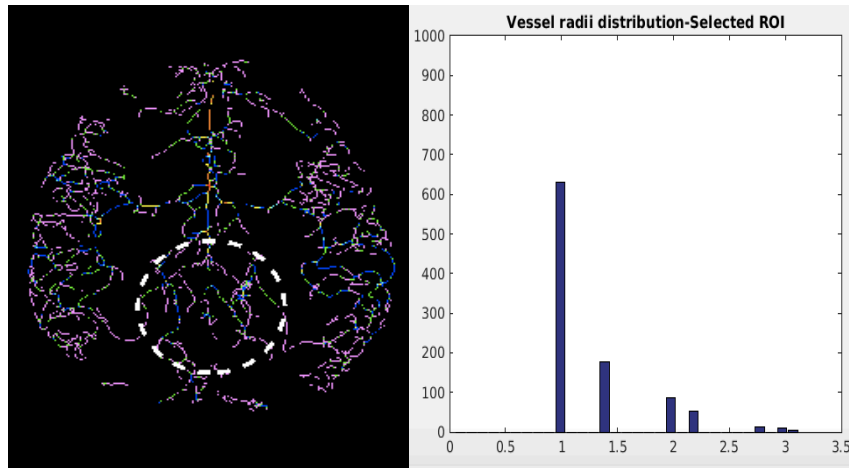
Figure 15: Vessel radii distribution for the different sub regions of the brain- ROI 2

Similarly, EDT was applied to the entire 3D volume as well as the continuous 8mm projected slices and Maximum Intensity Projection. The resultant images and their log histograms are shown in Figure 16. It is observed that the EDT on the 2D MIP has the maximum range of thickness, but the 3D spatial information is lost. Whereas for the EDT on the 3D volume, the range of thickness is limited, but good spatial information can be obtained. 8mm projections were a good balance between retaining 3D information and range of thicknesses.
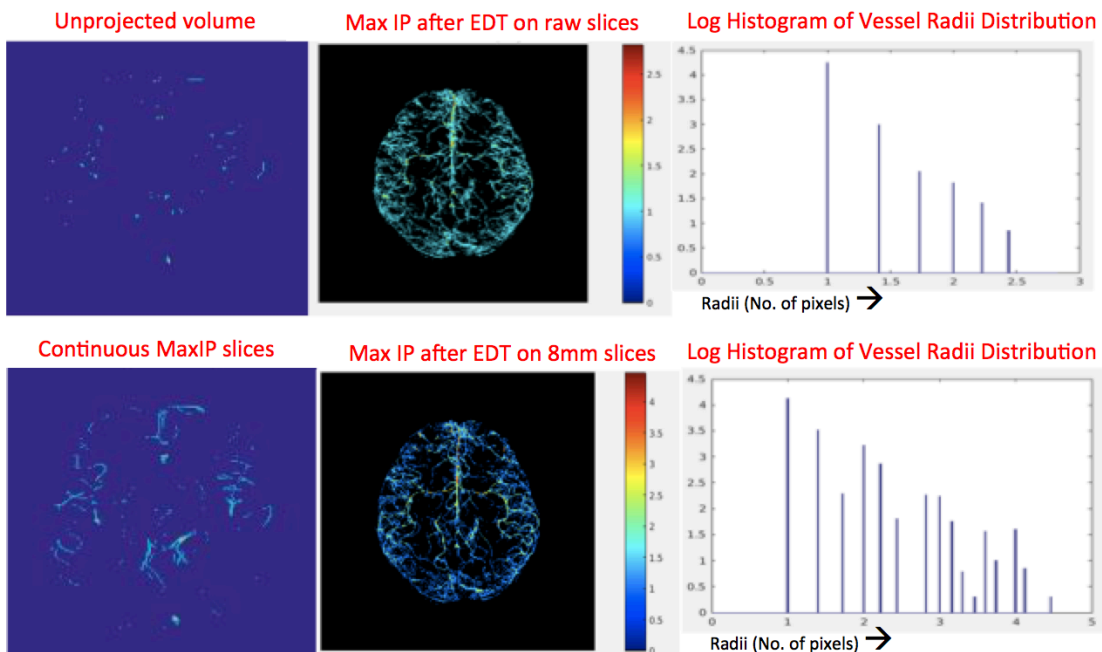

Figure 16: Effects of projection on EDT

The logarithmic histograms plotted in the same plot are shown in Figure 17(a). The difference between the two is plotted in terms of percentage variation as shown in Figure 17(b). This difference should be taken into account when making comparisons between serial scans.
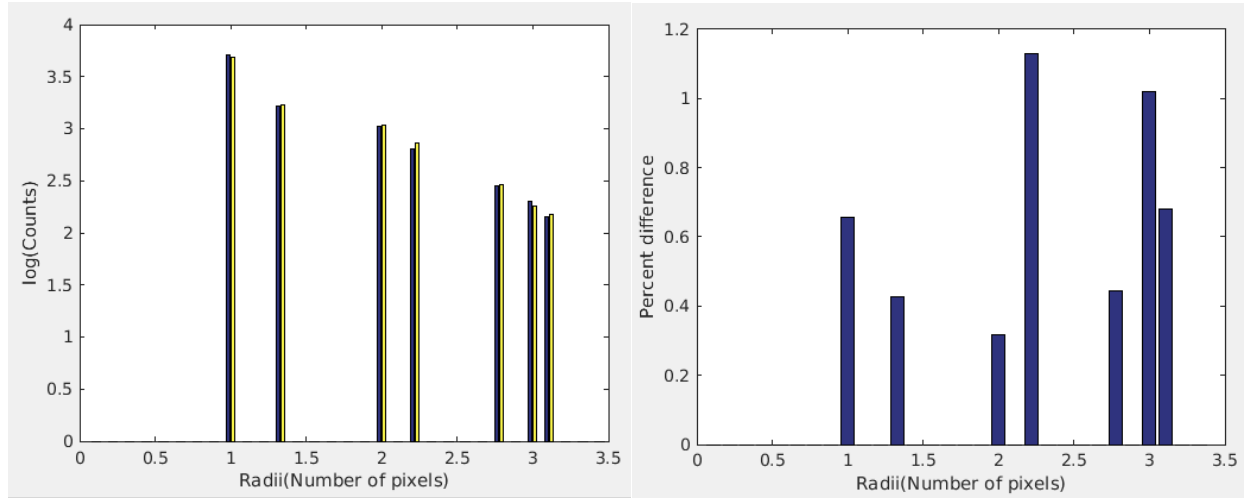

Figure 17(a): Vessel radii distribution for the 2 scans, scan1- yellow, scan2- blue (b) Difference between the 2 scans shown in percentage

3.4 Overlay of Vessel Thickness Map

The 2D vessel thickness map is then overlaid on the 2D MIP MRA and the resultant image is shown in Figure 18(left). Some of the small arteries are missing in the vessel thickness map because the thresholding algorithm was not effective in segmenting those small vessels. The overlay of vessel thickness map generated from an 8mm projected MRA slice on the corresponding SWI for a single 8mm continuously projected slice is shown in Figure 18(right). Since the Hessian method was sensitive to small vessels, we then combined the inner region from the Hessian filtered image and the outer region from the thresholded image as shown in Figure 19(left). In order to improve the display of the vessel thickness map, we then generated a skeleton from the Hessian method, where adaptive thresholding fails and assume a 1-voxel thickness for those segments. This combined vessel thickness map is shown in Figure 19(right).

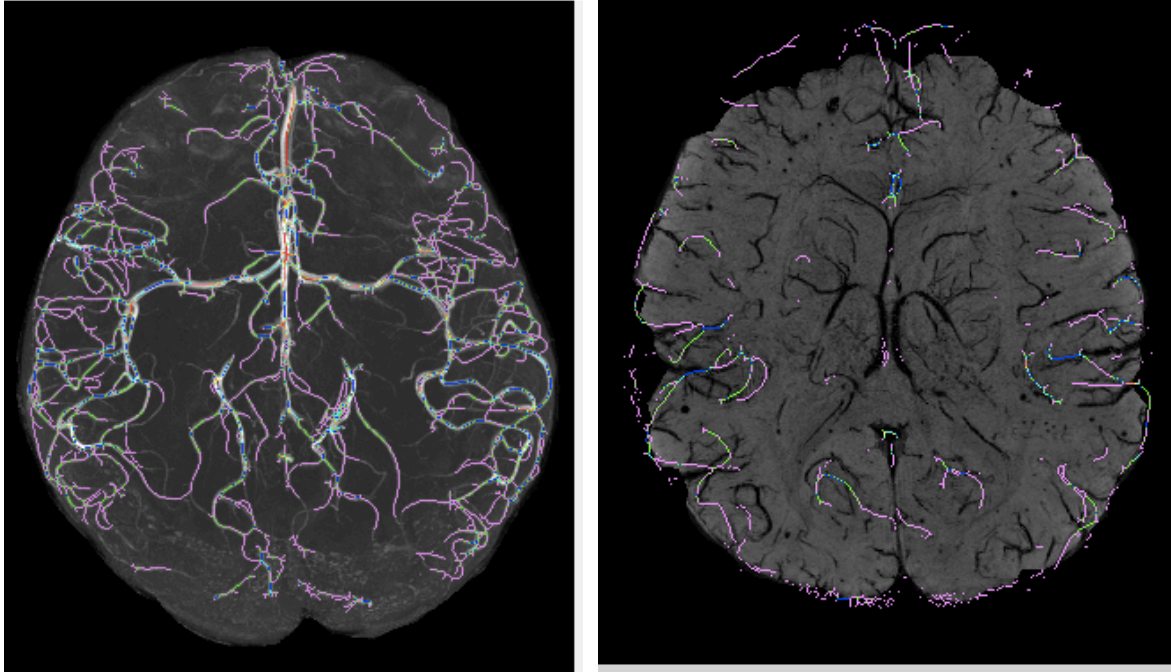**Figure 18 (left) 2D vessel thickness map is overlaid on the 2D MaxIP MRA (right) Overlay of vessel thickness on the corresponding SWI for a single 8mm projection**
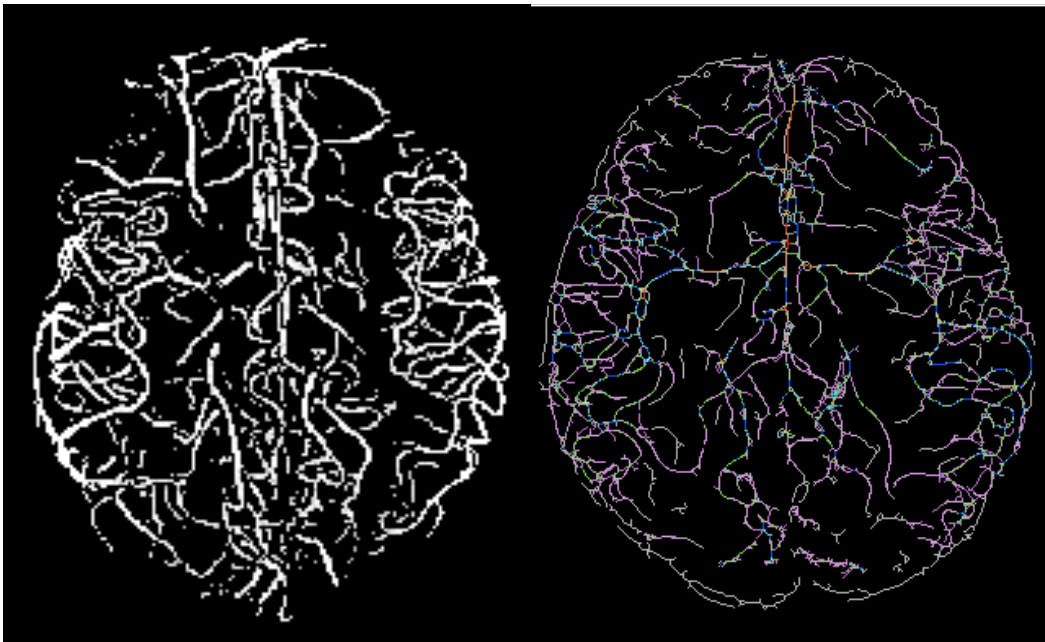

Figure 19(left) Combining inner region from Hessian filtered image and outer region from thresholded image (right) Combining vessel thickness map with results from low scale of Hessian filter skeleton (seen as gray in the image)

3.5 Preliminary Analysis of Vessel Thickness in Irradiated Children

Figure 20 shows the comparison between three females who are all 24 years old. As hypothesized, there is a shift in histogram towards the left as the time since radiation therapy increases. Even though the patients have similar age and received similar dose, the vessel radii distribution varies based on the time since radiation therapy.

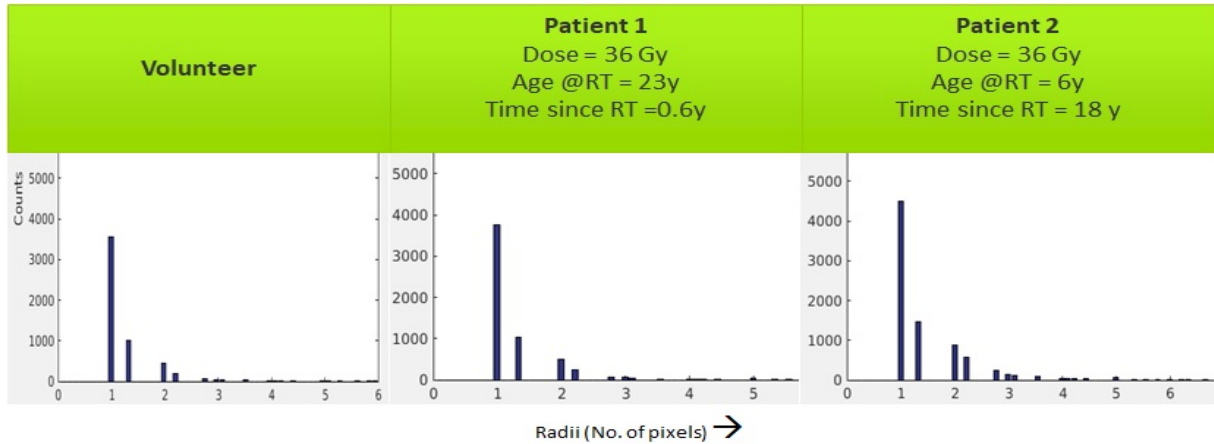**Figure 20: Vessel radii distribution for 3 subjects, all 24 years old**

Figure 21 shows the vessel radii distribution for three other irradiated children. Patient 3 has the most small vessels and the longest time since RT. This is an example of one type of analysis we are now capable of pursuing in the large population.
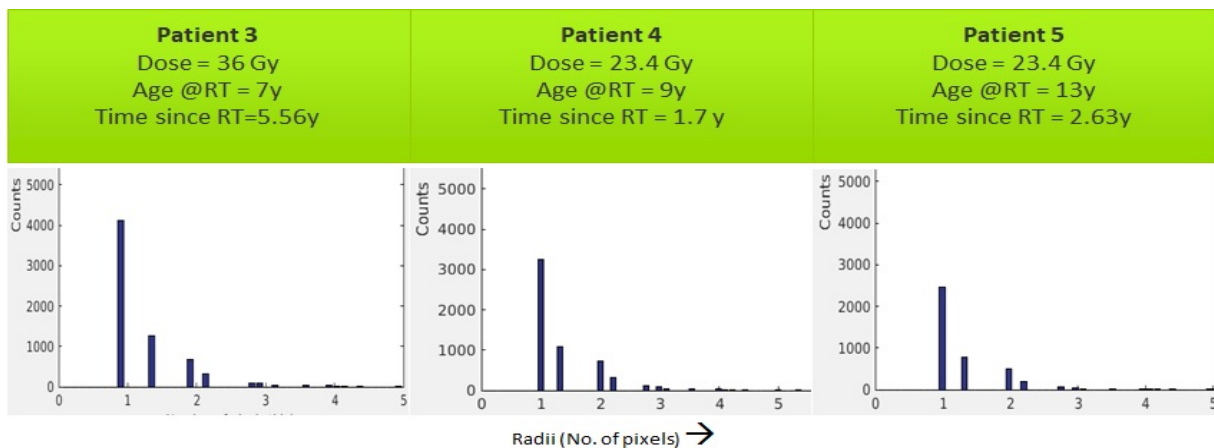

Figure 21: Vessel radii distribution for remainder of the subjects

CHAPTER 4

DISCUSSION

In general, the extraction of vessels is a complex process because of their tortuosity and branching. Due to partial volume averaging, a vessel can have a variety of intensity contributions from vessels and background. Particular difficulties occur at vessel bifurcations due to partial volume effects and calcification (which is common in bifurcations). The complexity of the vessel filtering increases with density and reduction of the diameter of vessels. The dynamic range of intensities is small between vessels and other objects. Despite the high resolution and contrast achievable with 7T MRA, we are still limited in comparison to the size of the microvasculature. Thus this approach cannot assess capillaries. Nevertheless, this method has the ability to provide quantitative in vivo whole-brain assessment of vessel number, radius and tortuosity for vessels that can be resolved by TOF-MRA. Analysis of the vasculature can be performed on the vasculature of the entire brain or any desired portion of the brain.

Since MRA assesses moving flow, it evaluates only blood flow through the lumen and hence the actual vessel wall thickness is not depicted in this study. The exact vessel radii can be measured only by histological analysis. However, an advantage of our method is its capability of non-invasively track changes in vasculature for an individual patient over time. A reduction in the number of vessels visualized by MRA can represent an absolute reduction in the number of vessels or indicate a reduction in blood flow (thereby making some vessels invisible to MRA although the vessels themselves might be physically present), or both.

One limitation stems from the fact that the thresholding algorithm was not effective in segmenting small vessels. The Hessian method on the other hand, was sensitive to small vessels, but can amplify noise and include the edges of the brain. By combining the inner region from the Hessian filtered image and the outer region from the thresholded image, better

visualization is possible. Our solution to improving the display of vessel thickness map was to combine it with results from the skeleton of the low scale Hessian filter. Another limitation of this work is that for comparison of two individuals, registration is not performed. In the future, rather than comparing two similarly aged subjects, registering to a normal vessel atlas would help in investigating group differences. Also, since brain volume differs between individuals, histogram counts of vessel thickness should be normalized based on the total brain volume imaged.

Future studies will involve longitudinal follow-up with serial imaging to investigate changes in vasculature due to treatment and correlate it with the number and location of CMBs. Analysis of global and focal histograms of thicknesses between different RT doses and as a function of time since RT in irradiated patients will also be investigated and correlated with microbleed size, distance, and time from RT. Other quantitative measures like vessel number, radius and tortuosity can also be calculated from the MRA images. Refining the adaptive thresholding algorithm based on the skeleton obtained from the Hessian method would also improve the segmentation of small vessels.

CHAPTER 5

CONCLUSION

Understanding the temporal evolution of the late effects of radiation therapy on the microvasculature and surrounding brain tissue is an important aspect in the management of children with brain tumors. This thesis provided tools for being able to quantify radiation-induced vascular injury in order to better understand the underlying mechanism of microbleed formation and ultimately how it affects cognition in the developing brain. This involved segmentation of arteries from TOF-MRA images, visualization with veins and CMBs from SWI images, and accurate quantification of vessel thickness. Although the Hessian method was effective in enhancing arteries for segmentation and visualization, it did not provide thickness information and amplified unwanted edges or noise. We then applied an adaptive thresholding method to overcome these limitations and to generate a vessel thickness map from which the vessel radii distribution can be obtained. Because this approach still missed lower contrast arteries, a combined approach worked best for both quantification and overlaying segmented arteries and thickness maps on SWI, which allowed for direct comparison among arteries, veins, and CMBs. Preliminary histogram analysis of vessel radii in a subset of patients and volunteers demonstrated its potential for larger scale analyses that investigate the affects of RT. We anticipate that the pipelines and display capabilities developed in this thesis will greatly facilitate future analyses that assess radiation-induced vascular injury in patients.

REFERENCES

[1] Pediatric Brain Tumors. (n.d). Retrieved from http://www.chop.edu/conditions-diseases/pediatric-brain-tumors

[2] 2016 CBTRUS Fact Sheet. (n.d). Retrieved from http://www.cbtrus.org/factsheet/factsheet.html

[3] Armstrong GT. Long-term survivors of childhood central nervous system malignancies: the experience of the Childhood Cancer Survivor Study. European journal of pediatric neurology: EJPN: official journal of the European Paediatric Neurology Society. 2010;14(4):298–303

[4] Mulhern RK, Palmer SL, Reddick WE, et al. Risks of young age for selected neurocognitive deficits in medulloblastoma are associated with white matter loss. Journal of clinical oncology: official journal of the American Society of Clinical Oncology. 2001;19(2):472–479

[5] Reeves CB, Palmer SL, Reddick WE, et al. Attention and memory functioning among pediatric patients with medulloblastoma. J Pediatr Psychol. 2006;31(3):272–280

[6] Robinson KE, Kuttesch JF, Champion JE, et al. A quantitative meta-analysis of neurocognitive sequelae in survivors of pediatric brain tumors. Pediatr Blood Cancer. 2010;55(3):525–531

[7] Taphoorn M, Klein M. Cognitive deficits in adult patients with brain tumors. Lancet Neurol. 2004;3(3):159–168

[8] Campen, C. J., Kranick, S. M., Kasner, S. E., Kessler, S. K., Zimmerman, R. A., Lustig, R., … Fisher, M. J. (2012). Cranial irradiation increases risk of stroke in pediatric brain tumor survivors. *Stroke; a Journal of Cerebral Circulation*, *43*(11), 3035–40

[9] Cole FM, Yates P. Intracerebral microaneurysms and small cerebrovascular lesions. Brain 1967;90:759–768.

[10] Roddy, E., Sear, K., Felton, E., Tamrazi, B., Gauvain, K., Torkildson, J., … Mueller, S. (2016). Presence of cerebral microbleeds is associated with worse executive function in pediatric brain tumor survivors. *Neuro-Oncology*, *18*(11), 1548–1558

[11] Radcliffe J, Packer RJ, et al. Three- and four-year cognitive outcome in children with non-cortical brain tumors treated with whole-brain radiotherapy. Ann Neurol. 1992;32(4):551–554

[12] Reimers TS, Ehrenfels S, Mortensen EL, et al. Cognitive deficits in long-term survivors of childhood brain tumors: Identification of predictive factors. Med Pediatr Oncol. 2003;40(1):26–34

[13] Aarsen FK, Paquier PF, Arts WF, et al. Cognitive deficits and predictors 3 years after diagnosis of a pilocytic astrocytoma in childhood. Journal of clinical oncology: official journal of the American Society of Clinical Oncology. 2009;27(21):3526–3532

[14] Reimers TS, Mortensen EL, Nysom K, et al. Health-related quality of life in long-term survivors of childhood brain tumors. Pediatr Blood Cancer. 2009;53(6):1086–1091

[15] CBTRUS Statistical Report: Primary brain and central nervous system tumors diagnosed in the United States, 2016. www.cbtrus.org

[16] Gutierrez, J., Cheung, K., Bagci, A., Rundek, T., Alperin, N., Sacco, R. L., … Elkind, M. S. V. (2015). Brain Arterial Diameters as a Risk Factor for Vascular Events. *Journal of the American Heart Association: Cardiovascular and Cerebrovascular Disease*, *4*(8), e002289

[17] Mazighi, M., Labreuche, J., Gongora-Rivera, F., Duyckaerts, C., Hauw, J. J., & Amarenco, P. (2009). Autopsy prevalence of proximal extracranial atherosclerosis in patients with fatal stroke. *Stroke*, *40*(3), 713–718

[18] Dury, R. J., Mason, S. L., Cicchetti, F., Drouin-Ouellet, J., Barker, R. A., Gowland, P. A., & Francis, S. T. (n.d.). Assessment of cerebral vascular abnormalities in Huntington's Disease at 7Tesla. ISMRM 2017

[19] Bian, W., Banerjee, S., Kelly, D. A. C., Hess, C. P., Larson, P. E. Z., Chang, S. M., … Lupo, J. M. (2015). Simultaneous imaging of radiation-induced cerebral microbleeds, arteries and veins, using a multiple gradient echo sequence at 7 Tesla. *Journal of Magnetic Resonance Imaging*.

[20] Ayaz, M., Boikov, A. S., Haacke, E. M., Kirsch, W. M., & Kido, D. K. (2010). Imaging cerebral microbleeds using susceptibility weighted imaging: one step toward detecting vascular dementia. *Journal of Magnetic Resonance Imaging : JMRI*, *31*(1), 142–148

[21] Greenberg, S. M., Vernooij, M. W., Cordonnier, C., Viswanathan, A., Al-Shahi Salman, R., Warach, S., … Breteler, M. M. (2009). Cerebral microbleeds: a guide to detection and interpretation. *The Lancet. Neurology*, *8*(2), 165–174

[22] Frangi, A. F., Niessen, W. J., Vincken, K. L., & Viergever, M. A. (1998). Multiscale vessel enhancement filtering. Medical Image Computing and Computer-Assisted Intervention, 1998

[23] Krissian K., Malandain, G., Ayache, N., Vaillant, R., Trousset, Y. Model Based Detection of Tubular Structures in 3D Images. Computer Vision and Image Understanding, Elsevier, 2000, Vol. 8, No.2,pp.130-171

[24] Sato, Y., Nakajima, S., Shiraga, N., Atsumi, H., Yoshida, S., Koller, T., … Kikinis, R. (1998). Three-dimensional multi-scale line filter for segmentation and visualization of curvilinear structures in medical images. *Medical Image Analysis*, *2*(2), 143–16

[25] Lorenz, C., Carlsen, IC., Buzug, T. M., Fassnacht, C., & Weese, J. (1997). Multi-scale line segmentation with automatic estimation of width, contrast and tangential direction in 2D and 3D medical images. In J. Troccaz, E. Grimson, & R. Mösges (Eds.), *CVRMed-MRCAS'97: First Joint Conference Computer Vision, Virtual Reality and Robotics in Medicine and Medical Robotics and Computer-Assisted Surgery Grenoble, France, March 19--22, 1997 Proceedings* (pp. 233–242)

[26] Bian, W., Hess, C. P., Chang, S. M., Nelson, S. J., & Lupo, J. M. (2013). Computer-aided detection of radiation-induced cerebral microbleeds on susceptibility-weighted MR images. *NeuroImage: Clinical*, *2*(1), 282–290

[27] Bradley, D., & Roth, G. (2007). Adaptive Thresholding using the Integral Image. *J. Graphics Tools*, *12*, 13–21

[28] Bullitt, E., Zeng, D., Mortamet, B., Ghosh, A., Aylward, S. R., Lin, W., … Smith, K. (2010). The effects of healthy aging on intracerebral blood vessels visualized by magnetic resonance angiography. *Neurobiology of Aging*, *31*(2), 290–300

Publishing Agreement

It is the policy of the University to encourage the distribution of all theses, dissertations, and manuscripts. Copies of all UCSF theses, dissertations, and manuscripts will be routed to the library via the Graduate Division. The library will make all theses, dissertations, and manuscripts accessible to the public and will preserve these to the best of their abilities, in perpetuity.

Please sign the following statement:

I hereby grant permission to the Graduate Division of the University of California, San Francisco to release copies of my thesis, dissertation, or manuscript to the Campus Library to provide access and preservation, in whole or in part, in perpetuity.

_____   _____
Author Signature   Date

9/11/17